RESEARCH ARTICLE

The Role of Ambient Turbulence in Canopy Wave Generation by Kelvin–Helmholtz Instability

W. D. Smyth[1] · **S. D. Mayor[2]** · **Q. Lian[3]**

Abstract

We test the hypothesis that internal waves observed in flow over forest canopies are generated by Kelvin–Helmholtz instability. The waves were observed at night, under stably stratified and weak wind conditions, with a horizontally scanning aerosol lidar and an instrumented tower. The lidar images are used to determine the salient wavelength and phase propagation velocity of each episode. Time series data measured at the tower are then used to form vertical profiles of background velocity and buoyancy just before each observed wave event. The profiles are input to the Taylor–Goldstein equation to predict the phase velocity, wavelength and period of the fastest-growing linear instability, and the results compared with the lidar observations. The observed wavelengths tend to be longer than predicted by the Taylor–Goldstein theory, typically by a factor of two. That discrepancy is removed when the theory is extended to account for the effects of ambient, small-scale turbulence.

Keywords Canopy waves · Instability · Kelvin–Helmholtz instability · Stable boundary layer · Turbulence

1 Introduction

Mean flows in the atmospheric boundary layer are often non-inflectional, i.e. there is no local maximum in the shear except at the boundary, and inflectional instability is therefore not expected (Smyth and Carpenter 2019), an example being the log layer (Kaimal and Finnigan 1994; Tong and Ding 2020). But a forest or other vegetation layer reduces the shear near the ground, producing a shear maximum near the treetop height. Turbulent coherent structures often observed in forest canopies are therefore thought to result from inflectional, or more specifically Kelvin–Helmholtz, instability (hereafter KHI; Kelvin 1871; von Helmholtz 1890;

✉ W. D. Smyth
   Bill.Smyth@oregonstate.edu

[1] College of Earth, Ocean and Atmospheric Sciences, Oregon State University, Corvallis, OR, USA

[2] Department of Earth and Environmental Sciences, California State University Chico, 400 West First Street, Chico, CA 95929, USA

[3] Guangdong Provincial Key Laboratory of Marine Disaster Prediction and Prevention, Institute of Marine Sciences, Shantou University, Shantou 515063, China

Raupach et al. 1996; Smyth and Moum 2012). Here we test this hypothesis by comparing wavelengths, phase velocities and periods of a subset of 53 wave events observed over an orchard canopy during stably stratified conditions with those predicted via linear stability analysis of flows measured at a nearby meteorological tower. We find that the test is successful only when the theory is extended to account for the ambient turbulence that is present just prior to observed wave events.

1.1 Canopy Waves

Studies of turbulence in forest canopies over several decades have revealed coherent structures with length scales on the order of the canopy height (Raupach and Thom 1981; Finnigan 2000). In unstable or neutral conditions, these appear to begin as rollers and to rapidly evolve into arch- and hairpin-shaped structures (Bailey and Stoll 2016). In stably stratified conditions, that evolution is suppressed, and internal waves with parallel bands of crests and troughs perpendicular to the mean flow are observed (Mayor 2017, hereafter M17).

For example, dramatic oscillations with wavelengths of order 100 m were observed in time series data measured over 20-m tall forest canopies at Camp Borden, Canada (Lee et al. 1996) and in Prince Albert National Park, Saskatchewan, Canada (Lee et al. 1997). Regarding the mechanical origin of such oscillations, it has been hypothesized that *"the turbulence and coherent motions near the top of a vegetation canopy are patterned on a plane mixing layer, because of instabilities associated with the characteristic strong inflection in the mean velocity profile."* (Raupach et al. 1996). In other words, canopy waves are believed to be created via the mechanism of KHI, which we describe next.

1.2 Kelvin–Helmholtz Instability

We begin with some definitions. The local atmosphere is measured by a Cartesian coordinate system in which $\{x, y, z\}$ are zonal (increasing eastward), meridional (increasing northward) and vertically upwards coordinates, $\{u, v, w\}$ are the corresponding velocity components. The background horizontal velocity is denoted $\mathbf{u}_h = \{\bar{u}, \bar{v}\}$. In our theoretical analyses, the overbar is taken to indicate a horizontal average. In the analysis of point data, as from a meteorological tower, it indicates a temporal average, here over a 5-min period.

Inflectional instability draws energy from the background flow at an inflection point of the background velocity profile or, more generally, at a local maximum of the shear magnitude:

$$S = \sqrt{\left(\frac{\partial \bar{u}}{\partial z}\right)^2 + \left(\frac{\partial \bar{v}}{\partial z}\right)^2}. \tag{1}$$

The instability mechanism is most easily understood as a constructive interference between vorticity waves that propagate horizontally above and below the inflection point and are therefore able to phase-lock (e.g.,Carpenter et al. 2013; Smyth and Carpenter 2019; Liu et al. 2022).

The resulting resonance creates exponentially growing plane wave structures in which departures from the mean state, e.g. $u' = u - \bar{u}$, have the form:

$$u'(x, y, z, t) = \left[\hat{u}(z)e^{\sigma t + \iota(kx + \ell y)}\right]_r, \tag{2}$$

where $\hat{u}(z)$ is a complex vertical structure function, σ is the complex growth rate, subscript r indicates the real part, and $\iota = \sqrt{-1}$. The wave vector $\mathbf{k} = \{k, \ell\}$ points horizontally. It may

also be represented in polar form in terms of its magnitude $\kappa = \sqrt{k^2 + \ell^2}$ and its direction $\phi = \tan^{-1}(\ell/k)$, measured counterclockwise from eastward. The wavelength is $\lambda = 2\pi/\kappa$, the phase propagation speed is $c = -\sigma_i/\kappa$ and the period is $\tau = \lambda/c$.

To optimize the inflectional instability process, the wave vector aligns with the background shear $\{\bar{u}_z, \bar{v}_z\}$ at the shear maximum. The phase speed lies between the minimum and the maximum of $\tilde{u}(z)$, the component of the background velocity profile in the direction of the maximum shear defined above (the semicircle theorem; (Howard 1961)). The wavelength of these plane waves scales with the thickness of the shear maximum where the instability is focused. For example, in an idealized shear layer $\bar{u} \propto \tanh(2z/h)$, where h is the layer thickness, the wavelength is approximately $7h$. The scale factor 7 can vary considerably, though, when the velocity profile has a more complicated form or when other effects are active.

KHI is the variant of the inflectional instability that occurs in a stably stratified fluid. That state is defined by the positivity of the squared buoyancy frequency, computed here as:

$$N^2 = \frac{g}{\overline{T}_v} \frac{\partial \overline{\Theta}_v}{\partial z}, \tag{3}$$

where g is the gravitational acceleration (here taken to be $9.81\,\text{m s}^{-2}$), $\overline{T}_v$ is the background virtual temperature and $\overline{\Theta}_v$ is the corresponding potential temperature. The gradient Richardson number is a dimensionless number that quantifies the strength of the shear relative to the stratification:

$$Ri = \frac{N^2}{S^2}. \tag{4}$$

The growth rate of the inflectional instability vanishes if the stratification is strong enough that the minimum gradient Richardson number, $\min_z\{Ri\}$, exceeds 1/4, i.e. the buoyancy frequency $N > S/2$ at all z (Miles 1961; Howard 1961). On the other hand, if the stratification is weak enough, the instability grows. The wave vector is aligned with the background shear vector as in unstratified flow, and the wavelength is only slightly modified. At large amplitude, the instability is manifested in trains of overturning billows that we call KH billows or (casually) KHI.

Stably stratified shear flows also support constructive interference involving gravity waves, leading to distinct mechanisms such as the Holmboe and Taylor-Caulfield instabilities (Smyth and Carpenter 2019; Arnqvist et al. 2016). These will not be considered here.

Because it grows on parallel shear flows with $\min_z\{Ri\} < 1/4$, we associate KHI with low Ri, i.e. strong shear and/or weak stratification. Moreover, as the instability grows to finite amplitude, it suffers a sequence of secondary instabilities that lead to a fully turbulent state (Klaassen and Peltier 1985, 1991; Caulfield and Peltier 1994; Mashayek and Peltier 2012a, b). We therefore expect to observe enhanced turbulence associated with KHI. As we will see, the observed canopy waves behave differently: they appear at times when Ri is not especially small, and turbulence is weak.

Stratified shear flows are subject to both viscous and diffusive effects (Thorpe et al. 2013). These need not be molecular in origin; they can also result from turbulence on scales much smaller than the instability, possibly left over from previous instabilities (Smyth et al. 2013; Kaminski and Smyth 2019). While the classical KHI model describes an infinitesimal disturbance growing on an otherwise parallel shear flow, natural flows almost always exhibit some degree of small-scale turbulence. Viscosity, either molecular or turbulent, tends to damp KHI in two ways: by directly retarding the unstable motions and by diffusing the background shear that drives them. Diffusion acts similarly to smooth out the instability, but its effect on

a stably stratified background flow is to reduce the stratification, thus enhancing the growth of the instability. Ambient turbulence generally varies with height, which can lead to more complex effects (Li et al. 2015).

1.3 Are Canopy Waves Created by KH Instability?

Because the inflectional instability mechanism results from constructive interference between waves above and below a shear maximum, it cannot occur when the shear maximum is at the ground, as in a standard logarithmic wind profile. However, vegetation can mix the background shear near the ground, creating an inflection point at which instability may grow. This suggests a possible explanation for the observed canopy waves (Raupach et al. 1996).

Analysis of the Saskatchewan canopy wave observations indicated that the waves were generated by shear near the top of the canopy (Lee 1997). Moreover, the observed waves shared some identifying features of KHI: their phase speed and direction were equal to the background wind near the center of the shear layer, and their amplitude decayed vertically away from that layer. Linear stability analysis confirmed that the observed profiles of velocity and density supported unstable modes. The computed growth rate, however, was not a maximum at the observed wavelength as would be expected.

A 20-m forest in Sweden produced inflectional flows and canopy waves that were well-described by KHI theory, even though tree drag and heat transfer were neglected (Arnqvist et al. 2016). In particular, the fastest-growing mode was identified and found to match the observed frequency. The interpretation suggested Holmboe-type instabilities (Sect. 1.2).

Although the connection between canopy waves and KHI is theoretically plausible and is consistent in many respects with existing observations, other processes, such as streamline displacement via wave-turbulence interactions (Sun et al. 2015) and the Jeffrey drag mechanism (Pulido and Chimonas 2001), can create waves in the forest environment. These mechanisms are alternatives to KHI for the creation of canopy waves.

1.4 The Canopy Horizontal Array Turbulence Study

The Canopy Horizontal Array Turbulence Study (CHATS; Patton et al. 2011) was conducted in 2007 to observe the fine-scale structure of turbulent flow over an idealized forest of uniform height and density. The experiment was conducted in a $1.6 \, \text{km}^2$ walnut orchard on flat terrain in Dixon, California, from mid-March through mid-June. The Raman-shifted Eye-safe Aerosol Lidar (REAL; Mayor et al. 2007) was deployed at a range of 1.61 km from a 30-m tall instrumented tower installed in the orchard. The average height of the trees was about 10 m and the nearly-horizontal lidar scans intersected the tower at an altitude of about 18 m above ground level.

Most observations of KHI in the lower atmosphere are made with radars (Richter 1969; Browning and Watkins 1970; Gossard et al. 1970; Chapman and Browning 1997), instrumented towers (Einaudi and Finnigan 1981; Finnigan et al. 1984; De Baas and Driedonks 1985), and sodars (Emmanuel et al. 1972; Hooke et al. 1973; Emmanuel 1973; Petenko et al. 2012). The observations are often limited to vertical profiles. To obtain 2D spatial data, which is necessary for the most reliable measurement of wavelength, scanning remote sensors are required. For example, Blumen et al. (2001) and Newsom and Banta (2003) describe an episode of turbulence associated with KHI observed in the stable boundary layer using a scanning Doppler lidar. In that work, the Doppler lidar scans provided vertical cross-sections of the waves from one event.
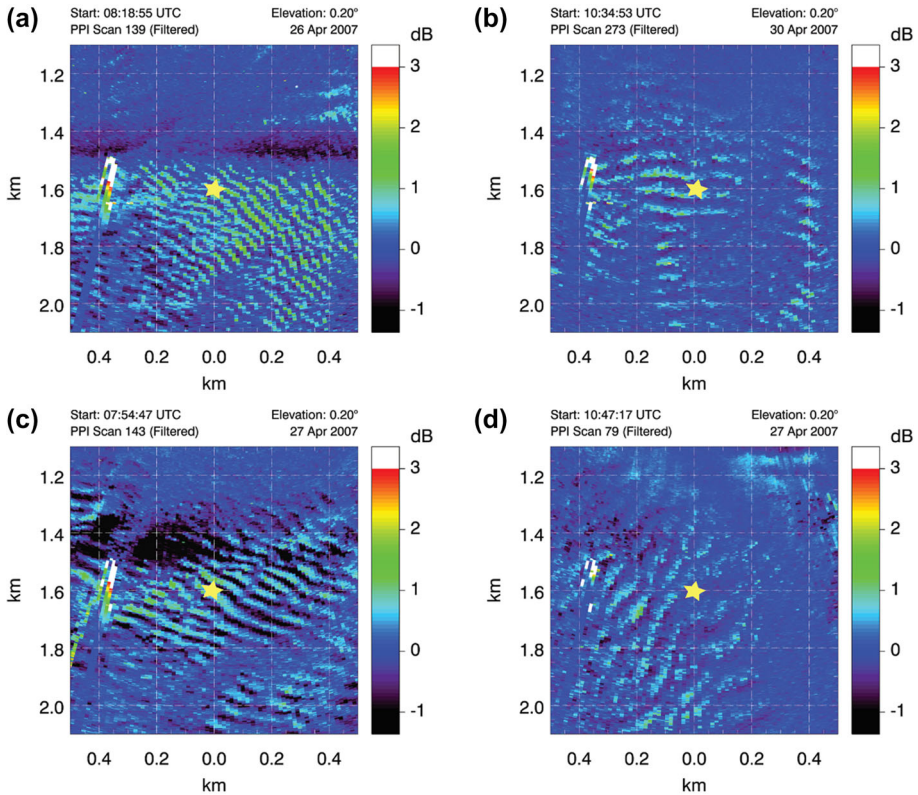
Fig. 1 Examples of canopy waves observed by the REAL during CHATS. In the labeling of M17 these are samples of events 16 (**a**), 24 (**b**), 19 (**c**), 20 (**d**). Each tile results from a single horizontal scan and shows a 1 km^2 area. The star in the middle of each panel indicates the position of the 30-m tower from which in situ data were obtained. White streaks on the left side of each image are the result of reflections from a few very tall trees

In our work (M17), the REAL was able to observe the waves on near-horizontal cross-sections and to capture 53 events over three months (Fig. 1). Graphical analysis of the images resulted in a wavelength assessment for 52 of these cases. The power and fast scan update rate of the REAL enabled the determination of the phase propagation velocity in 39 episodes where the lidar frame rate was fast enough to unambiguously determine wave crest displacement. We are not aware of any other atmospheric observational datasets that provide horizontal images of canopy wave spacing and phase velocity and coincident vertical profiles of thermodynamic and wind data. Herein we use these data to see how the prevailing KHI theory can be modified to link the observed vertical profiles and the wave characteristics revealed by the lidar.

During the 53 events identified by M17, a shear maximum was almost always found near $z = 10$ m, the nominal treetop height. Most of the horizontal lidar images intersect the tower (and therefore the vertical profiles) near 18 m height. Plane wave crests were nearly perpendicular to the background shear, consistent with the KHI theory outlined above. Moreover, waves propagated in the direction of the wind, and with about half the maximum wind velocity, consistent with the semicircle theorem (M17). Observed wavelengths were

Fig. 2 Vertical structure of shear and stratification just prior to observed wave events. **a** Median squared shear /4 (blue), squared buoyancy frequency (red). **b** Median gradient Richardson number. Solid curves represent the median of 5-min averages during observed events; dotted curves represent the quartiles. Horizontal solid lines show the nominal treetop height, $z = 10\,\mathrm{m}$; vertical dashed line on (**b**) shows $Ri = 0.25$
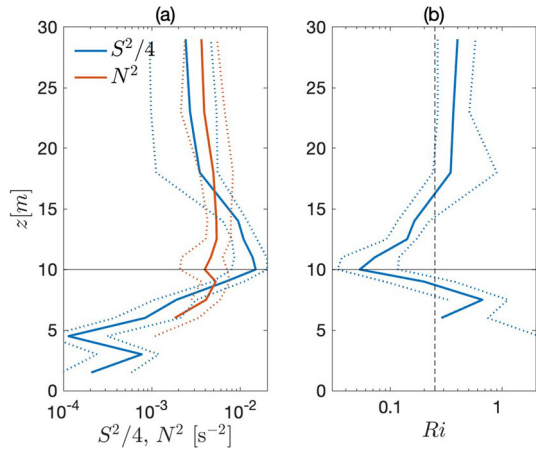
not evidently related to the length scale of the background shear, as is the case with KHI. As a first estimate, we may take the thickness h of the shear layer to be 3–5 m (M17), in which case the KHI wavelength estimate $7h$ becomes 21–35 m. In fact, based on the lidar images, the observed wavelengths ranged from 30 to 100 m, considerably longer than the theoretical estimate. That disparity is the primary motivation for the present study. We will argue that it results from ambient turbulence, which greatly affects the preferred wavelength of KHI.

1.5 Outline

The discussion is organized as follows. In Sect. 2 we composite the tower data to examine the evolution of the background flow, waves and turbulence over a diurnal cycle (Sect. 2.1) and over a canonical canopy wave event (Sect. 2.2). In Sect. 3 we use profiles of observed shear and density from the CHATS tower data, together with ambient turbulence having various assumed amplitudes, to calculate wave characteristics such as wavelength and phase velocity based on linear stability analysis. We then compare the results with observations from REAL. Conclusions are summarized in Sect. 4.

2 Evolution of the Mean Flow, Waves and Turbulence

In this section we examine the time-dependent relationship between KHI, canopy waves, turbulence and the evolving background state using composite representations of a diurnal cycle and of a canopy wave event. We also take an initial look at turbulent, or eddy, viscosity based on the tower data.

Fig. 3 Nocturnal probability density functions for the logarithm of **a** the minimum value of Ri and **b** the vertical velocity variance for $9 < z < 18$m and 19:00-07:00 local time. **c** Values measured over 5-min intervals immediately preceding canopy wave observations
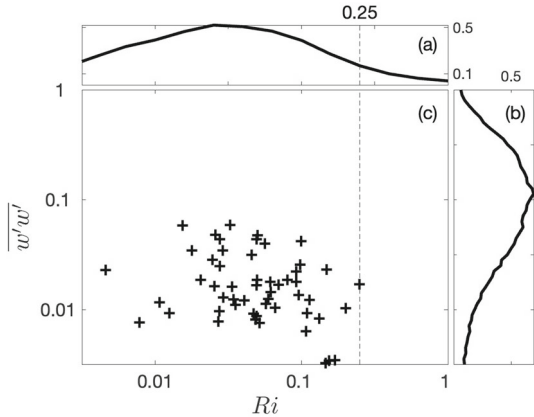
2.1 Flow Properties Prior to Canopy Wave Events

For each wave episode registered by REAL, a mean (or "background") state is defined by averaging tower measurements of wind velocity, temperature and humidity at over a 5-min period immediately prior to the appearance of the waves. In these states, the shear magnitude $S(z)$ is a maximum near $z = 10$m, coinciding with the nominal treetop height (Fig. 2a, blue curve). This height is also a local minimum of the squared buoyancy frequency N^2 and of Ri (Fig. 2b). The minimum of Ri is less than 1/4 just prior to all wave events (Fig. 3), consistent with KHI theory (Sect. 1.2). The layer in which $Ri < 1/4$ extends from slightly below $z = 10$m to approximately $z = 16$m.

The probability density function of Ri for nighttime data is unimodal with mode near 0.04 (Fig. 3a). Also unimodal was the vertical velocity variance $\overline{w'w'}$ (Fig. 3b). Canopy waves emerged only when Ri was less than 1/4 and $\overline{w'w'}$ was relatively small (Fig. 3c), indicating minimal small-scale turbulent transport despite the potential for KH instability.

2.2 The Composite Diurnal Cycle

Properties of the composite day (Figs. 4, 5, and 6) are educed by compositing the tower data recorded during each hour of the day for the 3-month duration of CHATS. For context, we begin by examining the upper level wind velocity, averaged over sensors at $z = 23$ and 29 m and over each instance of each hour. The meridional component (Fig. 4a, red curve) shows a diurnal variation with northerly flow from 04:00 to 14:30 LT and southerly flow at other times. This reversal coincides approximately with minima in the resultant averaged wind speed (blue). The zonal wind (Fig. 4a, yellow) is westerly and is relatively weak and steady.

The cause of the meridional wind reversal is the diurnal heating and cooling of California's Central Valley relative to the steadier marine airmass over the Pacific Ocean 100 km to the west (Zaremba and Carroll 1999). The California Coast Ranges separate the cool marine air from the diurnally changing inland air except for a gap in the San Francisco Bay area. Air entering the Central Valley through the gap (approximately 55 km to the southwest) moves northward over Dixon during the afternoon and evening until late night and early morning cooling in the Central Valley relaxes the horizontal pressure gradient enabling a northerly prevailing flow. The prevailing northerly flow is the result of the north–south orientation of the Central Valley and synoptic scale flow around a semi-permanent anticyclone that exists over this region.
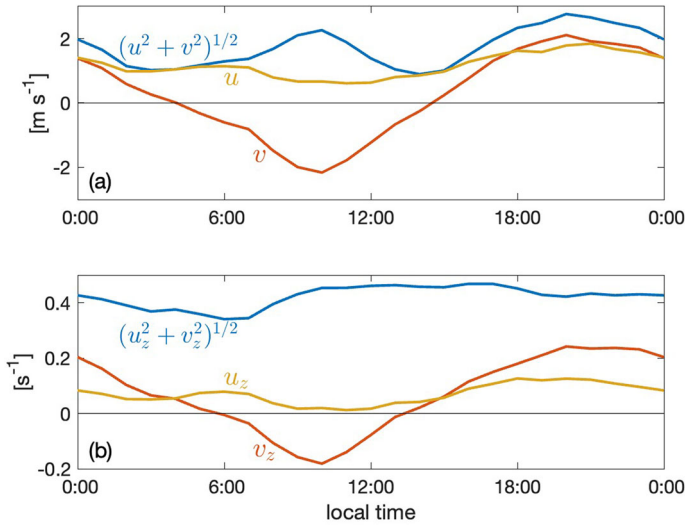
Fig. 4 Composite diurnal cycle of **a** upper level mean wind components (average of sensors at 23 and 29 m), and **b** mean shear components evaluated at the maximum of shear magnitude, $z = z_S$. Local time is UTC - 7 h. Subscripts in the curve labels indicate differentiation
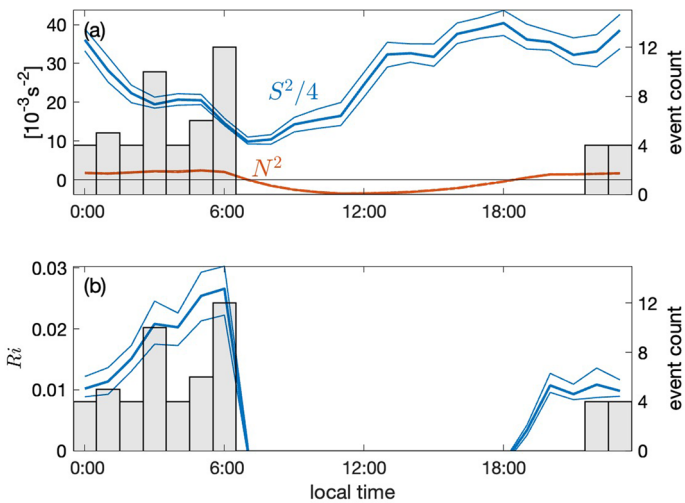

Fig. 5 Composite diurnal cycle of **a** the squared shear (/4) and buoyancy frequency, and **b** the gradient Richardson number, all evaluated at the shear maximum. Thick and thin curves indicate the median and its 95% bootstrap confidence limits, respectively, evaluated over the full 3-month observational period. Limits of the median N^2 are indistinguishable. Negative daytime values of Ri are not shown. Shaded bars, corresponding to the right-hand axis, indicate the number of wave events originating in each hour of the diurnal cycle

Evaluating the vertical derivatives $\partial \bar{u}/\partial z$ and $\partial \bar{v}/\partial z$ at the height where the shear magnitude is a maximum (usually near 10 m), and repeating the same compositing operations described above, we have the diurnal cycle of the shear magnitude and the zonal and meridional shear components (Fig. 4b). These vary similarly to the upper level winds: $\partial \bar{u}/\partial z$ (yellow curve) is weak and approximately constant while the dominant component $\partial \bar{u}/\partial z$
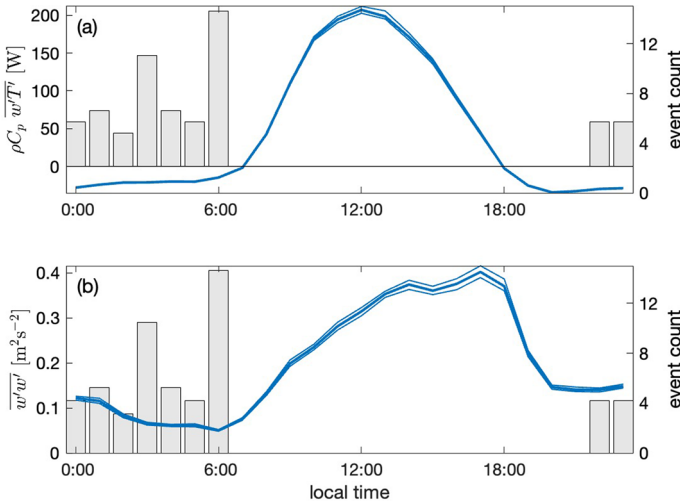
Fig. 6 Composite diurnal cycle of **a** the turbulent heat flux, **b** the variance of the vertical velocity component, each evaluated as the median over $9\,\mathrm{m} < z < 18\,\mathrm{m}$. Thin curves indicate the 95% bootstrap confidence limits in the median during each hour, evaluated over the full 3-month observational period. Shaded bars are histograms of the event count for each hour

(red) changes sign in the early morning and the early evening. The resultant shear magnitude (blue) decreased monotonically from midnight to sunrise, reaching an early morning minimum roughly coincident with the meridional shear reversal.

The squared buoyancy frequency N^2 (Fig. 5a), evaluated at the shear maximum, is considerably smaller than $S^2/4$, suggesting a strong likelihood of instability (Miles 1961; Howard 1961). During the day, N^2 dropped to near or below zero, indicating statically neutral or unstable conditions. Underlying the S^2 and N^2 curves on Fig. 5 is a histogram of the number of wave events observed in each hour of the REAL imagery. All observed events occurred at night, with event frequency increasing to a maximum at 06:00, just before sunrise.

This composite diurnal cycle presents some surprises. Ordinarily, we associate KHI with strong shear and weak stratification, or low Ri. But the present observations suggest a different scenario, in which instability is detected when shear is relatively *weak*, stratification is *strong* and thus Ri is *higher* than usual. Reflecting the variation of the shear, Ri is low during the day, rises rapidly around sunset and then more gradually to a maximum before dropping rapidly around sunrise (Fig. 5b, blue curve).

Contrary to the usual KHI model, wave events are *not* associated with the lowest Ri. Instead, the Miles-Howard criterion $\min_z \{Ri\} < 1/4$ is virtually always satisfied, usually by a large margin. In this near-homogeneous state, shear instabilities evolve rapidly and chaotically, transferring energy both downscale (as turbulence) and upscale (via vortex pairing; Winant and Browand 1974; Klaassen and Peltier 1989). Any recognizable monochromatic wave signal is quickly overwhelmed. Only when Ri increases to a moderate value can waves survive long enough to be detectable. Thus, waves are always detected at night and are more common toward sunrise when Ri is greatest.

The turbulent heat flux (Fig. 6a) was positive (upward) from approximately 07:00 to 18:00 LT and negative at other times.[1] The vertical velocity variance (Fig. 6b) increased

---

[1] The time of sunrise varied from approximately 07:30 to 05:45 during the observation period while sunset varied from 19:15 to 20:30.

steadily throughout the day, decreased rapidly around sunset, then decreased more gradually through the night. The peak event frequency at 06:00 coincides with the minimum vertical velocity variance, i.e., the *least-turbulent* ambient conditions. These observations suggest that the vertical motions revealed in the velocity variance and the heat flux (Fig. 6) are dominated not by the wavelike instabilities detected by REAL but rather by turbulence.

2.3 The Composite Canopy Wave Event

The composite event is formed by shifting the time during each canopy wave observation so that $t = 0$ when the waves are first visible in the REAL imagery. We then average over all 53 episodes and show the results from one hour before to one hour after the time of first visibility.

The upper level wind (Fig. 7a) does not change much in strength prior to wave emergence, though it changes in direction. The maximum shear (Fig. 7b, black curve, 7c, blue) trends downward, showing only a slight increase just before the event is observed. During the interval from -30 to -5 min., S^2 decreases by 31%. The buoyancy frequency changes very little (red); the increase from -30 to -5 min. is 9%. Decreasing shear and increasing stratification combine to create a 37% increase in Ri. In summary, the variables that normally govern inviscid KHI do not indicate any systematic change that would account for the emergence of instability at the particular time when it is observed. The change in the median long-wave radiative heat flux (Fig. 7e) is only $\sim$5%. Together with the relative steadiness of N^2 and Ri, this indicates that destabilization by radiative heating (Cava et al. 2004) is not a critical factor in these observations.

Of the variables examined here, the vertical velocity variance (Fig. 7f) shows the only change that could explain the appearance of instability, decaying by 32% prior to wave detection. We interpret this to suggest that, prior to wave emergence, instability is suppressed by ambient turbulence, and appears only when the latter has decayed sufficiently to permit sustained growth. The variance then increases rapidly as the wave signal grows.

2.4 Observational Estimates of Eddy Viscosity and Diffusivity Prior to Canopy Wave Events

The classical KHI theory is likely to be insufficient to explain these observations because the flow is turbulent before the instability sets in. The effect of this pre-existing turbulence is modeled most simply by choosing values for the corresponding eddy viscosity and turbulent diffusivity just prior to the onset of KHI.

Vertical eddy viscosity $A_v(z)$ and diffusivity $K_v(z)$ were calculated from the tower data via the relations:

$$A_v = -\frac{\bar{u}_z \, \overline{u'w'} + \bar{v}_z \, \overline{v'w'}}{S^2} ; \quad K_v = -\frac{\overline{T'w'}}{\bar{T}_z}, \tag{5}$$

where primes indicate departures from the 5-min mean. During the 5-min period preceding each of the 53 observed events, these values are typically between zero and $0.2\,\text{m}^2\,\text{s}^{-1}$ (Fig. 8a). Above the treetops ($z \approx 10\,\text{m}$), median values of eddy viscosity and diffusivity are similar, i.e. the turbulent Prandtl number is near unity, as is commonly observed in strong turbulence (the Reynolds hypothesis). Both coefficients decay smoothly upward from $z \approx 10\,\text{m}$. Below $z \approx 9\,\text{m}$, A_v and K_v are unequal and highly variable. It is likely that, in the well-mixed air near the ground, A_v and K_v are ratios of small quantities and are therefore
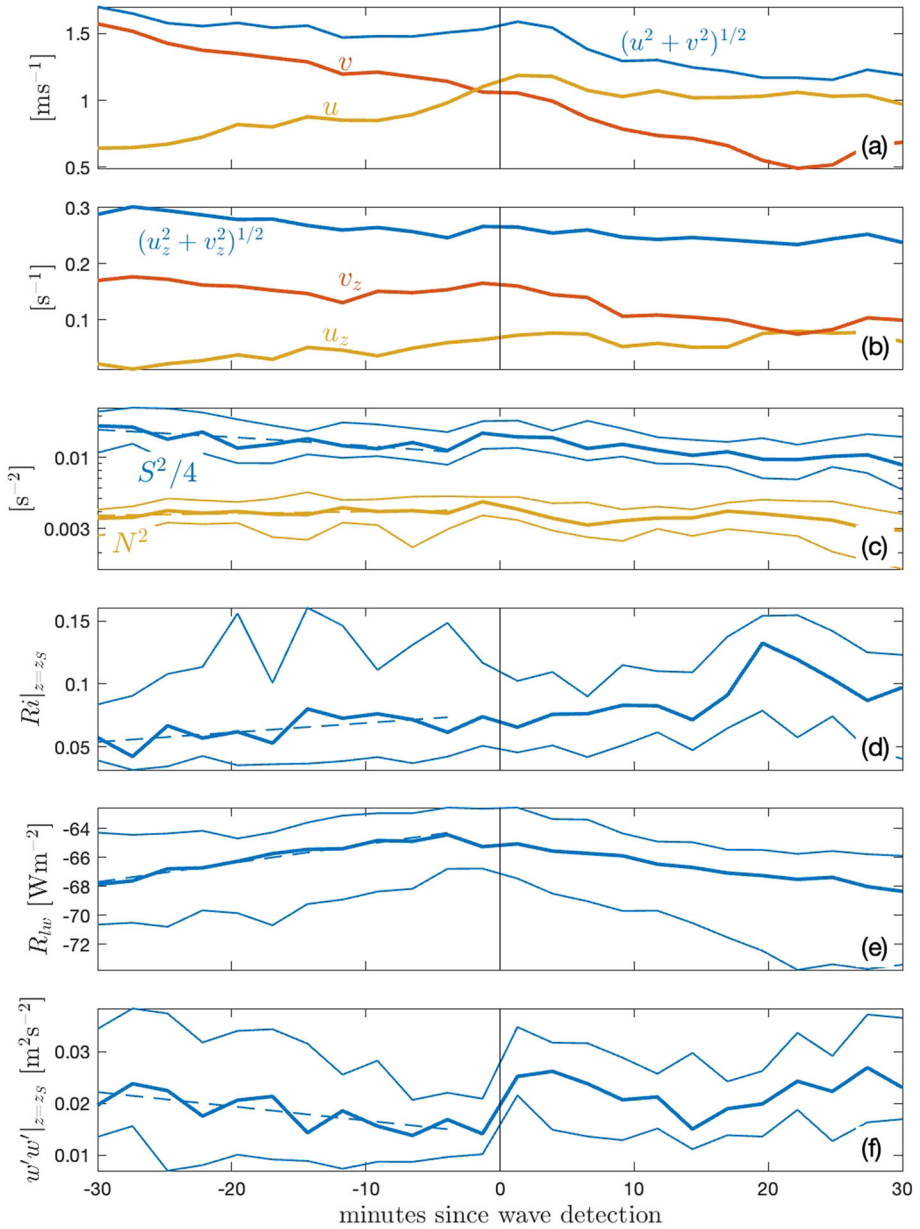
Fig. 7 Composite wave event, showing variables averaged in each 5-min period for 30 min before and after event detection. **a** Mean wind velocity; average of sensors at $z = 23$ m and 29 m. **b** Mean shear components and magnitude at the height of maximum S^2. **c** Median squared shear $/4$ and squared buoyancy frequency. (d) Median Ri at shear maximum. **e** Long-wave radiative flux at the ground. **f** Vertical velocity variance $\overline{w'w'}$ at the shear maximum. Thick and thin curves show the median and its 95% bootstrap confidence limits. Dashed lines show the least-squares fit to the median in the interval from 30 to 5 min prior to wave detection
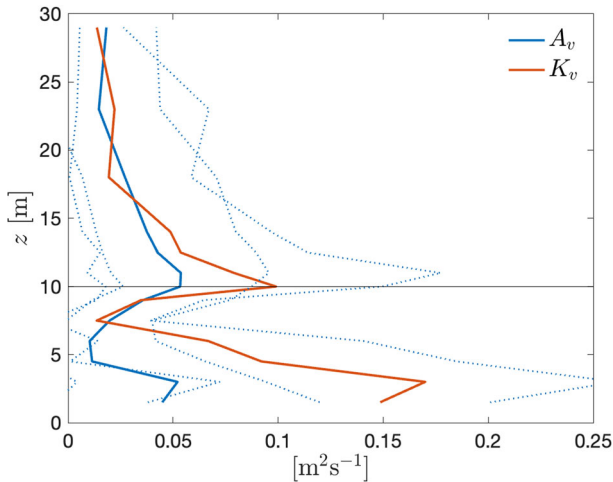
Fig. 8 Eddy viscosity (blue) and diffusivity (red) during the hour prior to observed wave events. Solid curves represent the median; dotted curves represent the quartiles. Horizontal solid line shows the nominal treetop height, $z = 10\,$m

highly uncertain. At all heights there is significant variation in A_v and K_v among different wave events. At the height of maximum shear, median values are $< A_v > = 0.05\,\mathrm{m^2\,s^{-1}}$ and $< K_v > = 0.09\,\mathrm{m^2\,s^{-1}}$.

Is this ambient turbulence sufficient to affect KHI? We will determine this explicitly later, but for now we consider a simple estimate based on the assumption of uniform A_v. Growth is affected significantly when the Reynolds number $\mathrm{Re} = h\Delta u/A_v$ is smaller than $\sim O(10^2)$, and is arrested entirely when $\mathrm{Re} < O(10)$ (Maslowe 1973; Smyth et al. 2013). If we take a typical velocity scale Δu to be $1\,\mathrm{m\,s^{-1}}$ and the layer thickness to be $4\,$m, then $\mathrm{Re} = 100$ corresponds to $A_v = 0.04\mathrm{m^2\,s^{-1}}$, similar in magnitude to the median measured value at treetop height quoted above. The condition $\mathrm{Re} < 10$, required to stabilized KH instability, requires $A_v > 0.4\mathrm{m^2\,s^{-1}}$. We therefore expect that eddy viscosity associated with ambient turbulence (Fig. 8) will have a significant damping effect on the growth of KH instability, but will not stabilize it entirely.

In the remainder of the paper, we demonstrate that ambient turbulence has a significant effect on the growth of the observed instabilities. For simplicity in this initial investigation, we assume that ambient turbulence is stationary, homogeneous and isotropic.

3 Comparison of Observed Canopy Waves with KHI Via Linear Stability Analysis

We now ask whether the observed canopy waves could have been generated by KHI. To answer this, we perform explicit linear stability analysis of the mean profiles measured just before each wave event. We predict the phase speed, direction and wavelength for each event and compare the results with the available observations from REAL. We also explore the possibilities that KHI is modulated by pre-existing turbulence or by air-vegetation fluxes. The following two subsections give details of our methods for deriving wave parameters via the REAL imagery (subsect. 3.1) and via linear stability analysis (subsect. 3.2). Results of the comparisons are in subsect. 3.3.

3.1 Estimating Wave Parameters from REAL Imagery

In Fig. 1 we show $1\,km^2$ areas from horizontal scans of the REAL from four sample canopy wave episodes. A full description of how the lidar data were collected and processed and the wave characteristics were extracted is contained in M17. To summarize the final steps, wave characteristics were obtained graphically by projecting the images on to a whiteboard and hand tracing the wavecrests. Wavelength was determined by measuring the average distance between two crests in the vicinity of the tower. Phase propagation speed was determined by observing the displacement of a wave crest over sequential scans, while the direction was by definition normal to the wave crests.

Figure 1 reveals the significant variability that exists among cases, as well as the spatial variability that may occur in a single image. In some cases, if the waves were not clear at the location of the tower, the measurement was made as close to the tower as possible. If the wave characteristics changed over time, an average was chosen. The goal of the analysis was to assign a single value of wavelength and phase velocity for each episode. A first attempt to determine a single wavelength and orientation per image objectively by computer algorithm was recently reported by Mifsud et al. (2021) and the results support the subjective values used in M17 and herein.

3.2 Linear Stability Analysis

KHI is obtained as a solution of the Taylor–Goldstein (hereafter TG) equation, which describes normal mode disturbances (defined in Sect. 1.2) evolving on an inviscid, stratified, parallel shear flow. The theory has been extended to include viscosity and diffusivity due to ambient small-scale turbulence (Liu et al. 2012; Lian et al. 2020), and to approximate the momentum and heat fluxes between the flow perturbation and the vegetation (Lee 1997). The Appendix describes the basic theory and methodology; here, we describe modifications unique to the present project.

For small perturbations from the background flow, the momentum exchange with the trees (e.g.,Lee 1997) is approximated by an acceleration $-C_d L_f \sqrt{\bar{u}^2 + \bar{v}^2}\,\mathbf{u}'$. The constant C_d is a drag coefficient, typically set to 0.15, while $L_f(z)$ is the leaf area density. Based on the CHATS measurements (Patton et al. 2011), we assume a piecewise-linear form for L_f:

$$L_f(z) = \frac{5}{h} \begin{cases} 0, & z > h \\ (h-z)/(h-z_{\max}), & z_{\max} < z < h \\ z/z_{\max}, & 0 < z < z_{\max} \end{cases} , \qquad (6)$$

with tree height $h = 10\,m$ and $z_{\max} = 8m$. The rate of heat transfer from the trees is modeled similarly as $-C_h L_f \sqrt{\bar{u}^2 + \bar{v}^2}\,b'$, where $b' = -g\rho'/\bar{\rho}$ is the buoyancy perturbation and $C_h = 0.10$.

We assume that the ambient turbulence is homogeneous, isotropic and has unit Prandtl number so that the viscosities and diffusivities that work on vertical and horizontal gradients, A_v, A_h, K_v and K_h, are all uniform and equal to a constant A_0. Modifications to the classical TG problem are therefore quantified by the three parameters C_d, C_h and A_0. Their values are chosen using four models:

#1 First, fluxes of heat and momentum due to molecular motions, turbulence, and interactions with vegetation are all neglected, i.e. $C_d = C_h = A_0 = 0$. This results in the classic TG equation for a stratified shear flow (Smyth and Carpenter 2019).

#2 Next, we add fluxes of momentum and heat between the air and the vegetation with coefficients $C_d = 0.15$ and $C_h = 0.10$ following Lee (1997).

#3 Third, we retain $C_d = 0.15$ and $C_h = 0.10$ but add eddy viscosity/diffusivity with a fixed value $A_0 = 0.06\text{m}^2\text{s}^{-1}$, a compromise between the observational estimates of A_v and K_v at treetop height (Fig. 8).

#4 Finally, we determine for each case the value of A_0 that maximizes agreement between the computed wave vector of the fastest-growing mode and the estimate based on the REAL imagery (see subsect. 3.1). We repeat the calculation of the fastest-growing mode for a range of values of A_0 between zero and 0.4, then choose the A_0 that minimizes the difference in wave vectors. This model also retains $C_d = 0.15$ and $C_h = 0.10$.

We solve these models using as input profiles of horizontal velocity and buoyancy obtained from the CHATS tower measurements. For each of the 39 observed events for which wave parameters have been measured, the corresponding mean state is identified as the velocity and buoyancy profiles obtained by averaging in time over the 5-min period immediately preceding the first appearance of the billows in the REAL imagery. The 5-min averaging interval is intended to be long enough to average out the slowest observed wave periods (60 s) yet short enough to preserve fluctuations in the mean flow that create instability. To maintain the validity of the normal mode solution form, only modes with growth rate faster than $1/(5\,\text{min}){=}0.033\,\text{s}^{-1}$ are retained. Wind above the uppermost measurement at 29 m is assumed to vary linearly, thus ensuring that $U_{zz} = V_{zz} = 0$ and avoiding spurious shear instabilities. The buoyancy frequency is assumed to be constant above 29 m.

Generalizing the approach of Lee (1997), we make no assumption about the wavenumber and propagation direction but instead scan over those parameters to identify the fastest-growing instability. Wave properties, including speed and direction of phase propagation, wavelength and period are compared with estimates based on the REAL observations described in M17 (details in subsect. 3.1). By investigating not just a single case but instead 39 cases in which waves were observed, we are able to draw general conclusions about the validity of the linear model.

3.3 Results

We first describe a representative case that illustrates the methods and the main results. We then generalize the results via a statistical analysis of 39 events for which clear observations of canopy wave parameters are available.

3.3.1 Case Study: Event #40

To illustrate the analysis, we first examine event #40 (in the numbering of M17), which began at 03:33:34 LT (local time is URL - 7 h) on 2 June 2007 and lasted for 6 min, 10 s. The background velocity profile (Fig. 9a) may be crudely described as a shear layer between ~ 5 m and ~ 23 m in which the wind increased from near zero to ~ 2 m/s from the WSW.

The mean squared shear profile (Fig. 9b, blue curve) shows a sharp maximum at 10 m. The squared buoyancy frequency (Fig. 9b, red curve) is generally positive but is, importantly, less than $S^2/4$ (implying $Ri < 1/4$) between 8 m and 23 m. The shear maximum at 10 m is accompanied by a stratification minimum (suggesting previous mixing) and thus very low Ri. The flow is therefore potentially unstable to shear-driven instabilities.

We now solve the stability problem for a range of wave vectors $\{k, \ell\}$ and plot the growth rate σ of the fastest growing mode at each point (Fig. 9c). For this illustrative calculation, we
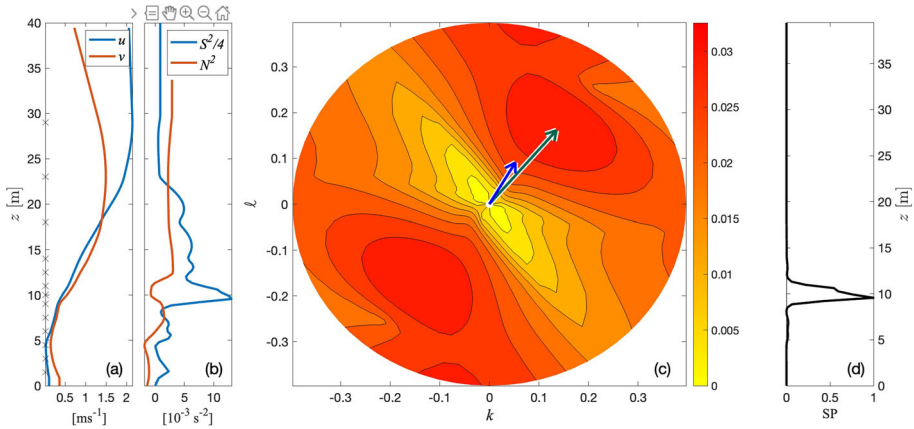
Fig. 9 LSA of event #40 (2 June 2007, 10:33:34-10:39:44 UTC). **a** Mean velocity profiles. Measurement heights are marked on the vertical axis. **b** Squared shear and buoyancy frequency. $Ri < 1/4$ when $S^2/4 > N^2$. **c** Growth rate versus zonal and meridional wave vector components. Blue arrows indicate the observed wave vector; black arrows highlight the wave vector of the fastest-growing instability, $\kappa = 0.2\,\mathrm{m}^{-1}$, $\phi = 50°$. **d** The shear production rate (normalized by its maximum value)

use the TG model (#1 in Sect. 3.2). Instability is found over a broad range of wave vectors, with maximum growth rate $0.033\,\mathrm{s}^{-1}$ at $\kappa = 0.2\,\mathrm{m}^{-1}$ (i.e. wavelength 30 m) and direction 50° north of east. At this growth rate, the disturbance grows by a factor e in about 30 s. The period in which the waves are observed to grow includes several of these e-folding intervals, showing that the growth rate is sufficient to explain the observations. Note also that the time scale for instability growth is much faster than the 5-min averaging interval that defines the background flow. We are therefore justified in using the normal mode solution form (2). If this were not true we would reject the result.

The lower half of Fig. 9c is a reflection of the upper half due to the symmetry of the equations. The black arrow indicates the fastest-growing mode over all $\{k, l\}$. The indeterminacy in the wave vector of the fastest-growing mode due to the aforementioned symmetry is resolved by requiring that the phase propagation speed c be positive. The shear production rate (Fig. 9d) for this mode is sharply peaked near $z = 10$m, confirming that the instability draws its energy from the shear just above the treetops.

The blue arrow in Fig. 9c indicates the wave vector as measured graphically from the REAL imagery. Comparing the arrows, we see that the linear analysis predicts the direction of the wave vector quite accurately, but overestimates its length. More specifically, the observed wavelength of the billows is about twice that predicted by the stability analysis.

The calculation shown in Fig. 9 has been simplified by the omission of ambient turbulence effects and drag and heat transfer due to the leaves (i.e., model #1). We now ask how the result will change when those effects are accounted for. We first add the vegetation terms as specified in model #2, with coefficients $C_d = 0.15$ and $C_h = 0.10$. The result is shown in Fig. 10a. The main difference is an overall reduction in the growth rate; the maximum drops from $0.033\,\mathrm{s}^{-1}$ in the TG limit to $0.027\,\mathrm{s}^{-1}$ with the transfer terms included. The wave vector of the fastest-growing mode is virtually unchanged.

We next add eddy viscosity and diffusivity, with $A_0 = 0.03\,\mathrm{m}^2\,\mathrm{s}^{-1}$. The growth rate distribution now changes markedly (Fig. 10b). (Note that the axes have been altered from Fig. 9 to make the central region of the plot more visible.) At large wavenumbers (around the outside of the diagram), growth rates are greatly reduced. The two large regions of instability have
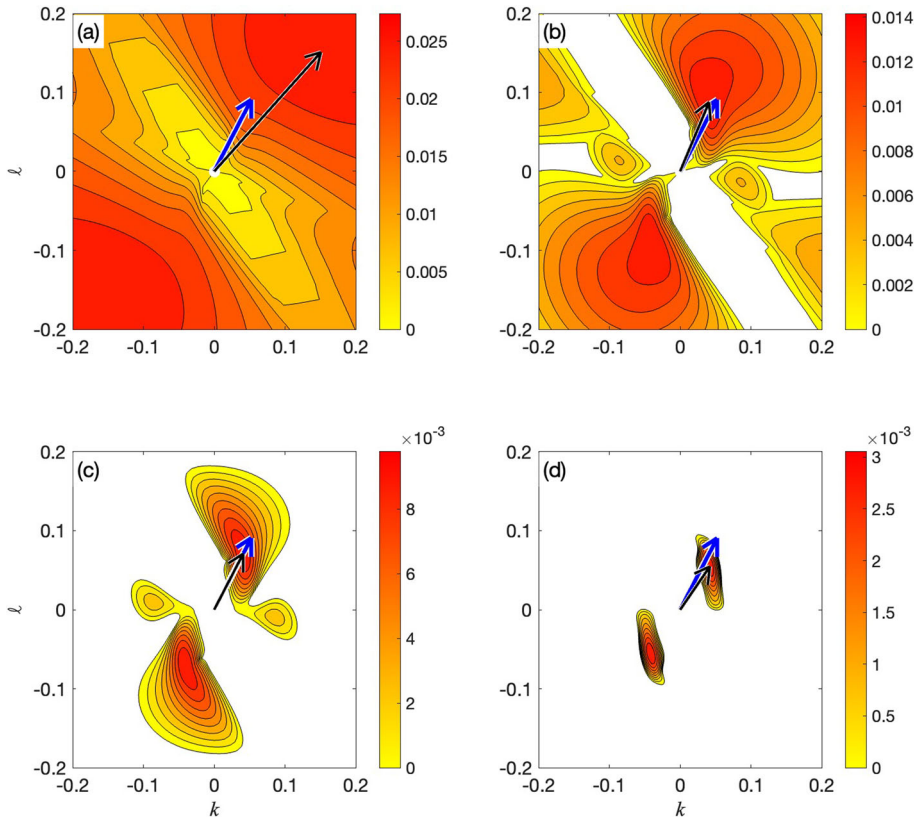
Fig. 10 Growth rate versus zonal and meridional wave vector components for event #40 with eddy viscosity/diffusivity amplitude $A_0 = 0$ (**a**), $0.03\,\mathrm{m^2\,s^{-1}}$ (**b**), $0.06\,\mathrm{m^2\,s^{-1}}$ (**c**) and $0.17\,\mathrm{m^2\,s^{-1}}$ (**d**). Arrows identify the fastest-growing unstable mode (black) and the observed wave vector (blue). In all cases $C_d = 0.15$ and $C_h = 0.10$

moved inward, indicating that smaller-wavenumber features are less vulnerable to viscous damping. The fastest-growing instability (black arrow) now has a wave vector quite similar to the observation (blue arrow).

We now repeat the experiment with A_0 increased to $0.06\,\mathrm{m^2\,s^{-1}}$ (model #3), and then to $0.17\,\mathrm{m^2\,s^{-1}}$. As shown in Fig. 10c and d, the region of fastest growth continues to move toward smaller wavenumbers (i.e. longer waves). The final eddy viscosity shown, $0.17\,\mathrm{m^2\,s^{-1}}$, yields a growth rate of $0.03\,\mathrm{s^{-1}}$, beyond which the time scale for instability growth is longer than the 5-min time scale of the background flow and the normal mode solution is no longer valid.

In Fig. 11, the wave vector predicted for $A_0 = 0.03\mathrm{m^2\,s^{-1}}$ is shown by an arrow superimposed on the REAL image for event #40. The reader may verify the correspondences in both magnitude (or wavelength) and orientation.

Figure 12 gives a more thorough depiction of the dependence of wave properties on the assumed eddy viscosity A_0. The growth rate (Fig. 12a) decreases monotonically with increasing A_0. The wavenumber κ (Fig. 12b) decreases sharply as A_0 is increased from zero, then becomes independent of A_0 at higher values. The dependence of ϕ on A_0 (Fig. 12c) is less consistent, but the prediction generally remains within a few degrees of the observed value. The phase speed (Fig. 12d) increases rapidly then flattens out at a value close to the observations.

Fig. 11 Example backscatter image from REAL, event #40 (2 June 2007, 10:33:34-10:39:44 UTC). The arrow indicates the wavelength and direction of propagation predicted by the linear stability analysis with $C_d = 0.15$, $C_h = 0.10$ and $A_0 = 0.03\,\text{m}^2\,\text{s}^{-1}$ (model #4). Thin vertical streaks result from the laser beam illuminating occasional elements of foliage
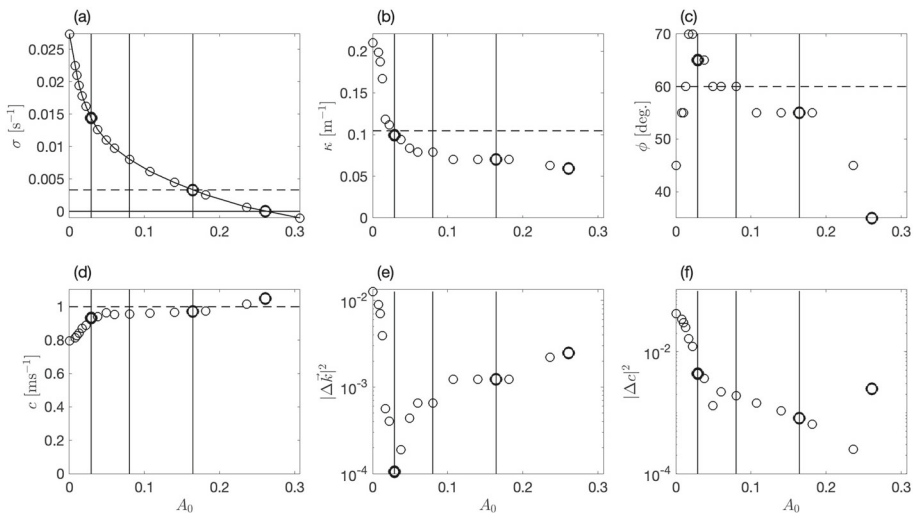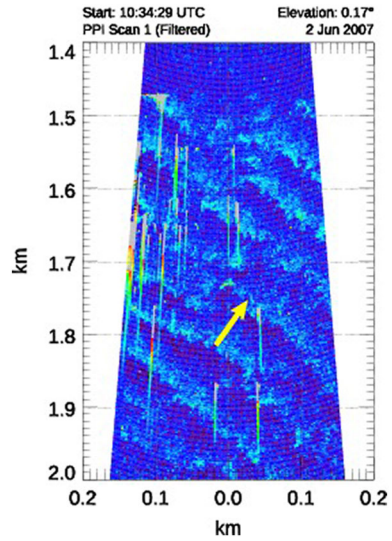

Fig. 12 (a–d) Properties of the fastest-growing instability versus A_0 for event #40: **a** growth rate σ, **b** wavevector magnitude κ, **c** propagation angle ϕ, **d** phase propagation speed c. The horizontal dashed line marks (**a**) the minimum growth rate consistent with the frozen-flow assumption, (**b,c,d**) the observed value. **e**: Squared magnitude of the difference between the wave vectors **k** of the computed fastest-growing instability and of the observed canopy wave. **f**: As (**e**) but for the phase propagation speed c. Vertical lines mark cases shown in Fig. 10: $A_0 = 0.03\,\text{m s}^{-1}$, at which the discrepancy in the wave-vector is minimized (cf. e), $A_0 = 0.08\,\text{m s}^{-1}$ and $A_0 = 0.17\,\text{m s}^{-1}$ (cf. a). In all cases $C_d = 0.15$ and $C_h = 0.10$

The discrepancy in the wave vector (Fig. 12e) shows a clear minimum at $A_0 = 0.03\,\text{m}^2\,\text{s}^{-1}$, the value used for Fig. 10b. The discrepancy in the phase speed (Fig. 12f) also drops rapidly with the introduction of eddy viscosity, decreasing by an order of magnitude at $A_0 = 0.03\,\text{m}^2\,\text{s}^{-1}$.

The stability boundary, at which the growth rate drops to zero due to strong eddy viscosity, is of interest although it is not formally valid as it violates the frozen flow assumption. In
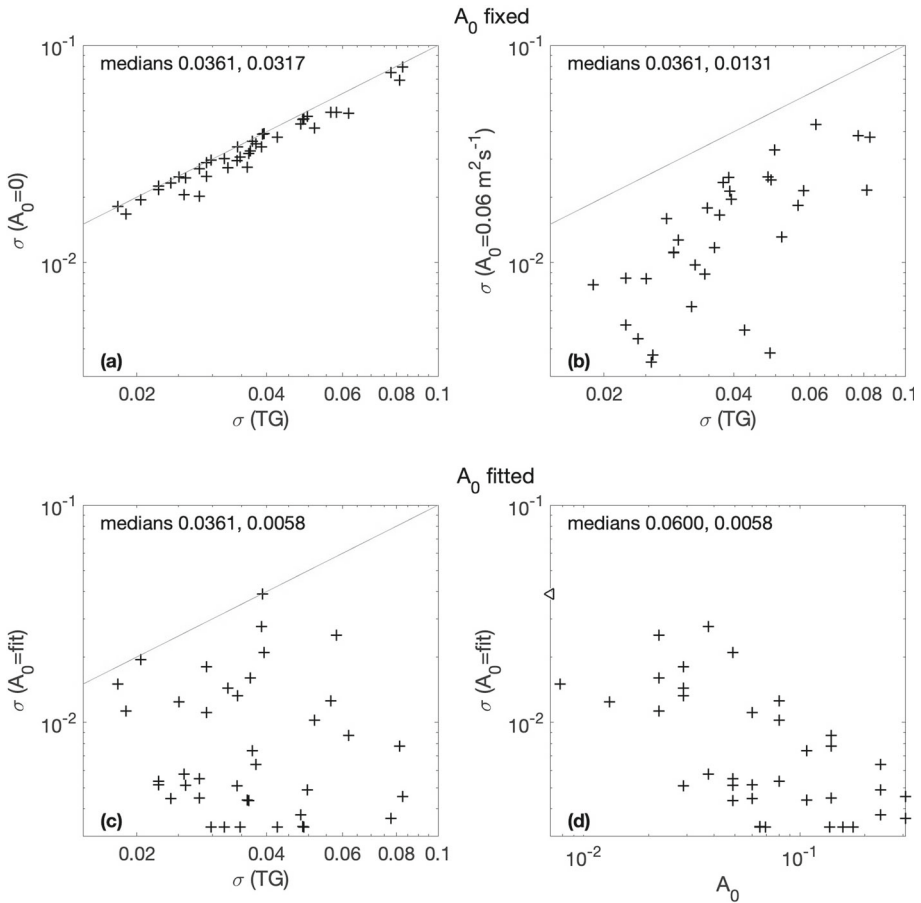
Fig. 13 Growth rates from the linear stability analysis of 39 observed wave events. Models including fluxes due to vegetation and ambient turbulence are compared with the original TG equation: **a** model #2, with air-tree fluxes following (Lee 1997), **b** model #3: air-tree fluxes plus turbulence with eddy viscosity/diffusivity $A_0=0.06\,\mathrm{m^2\,s^{-1}}$, **c** model #4: air-tree fluxes plus turbulence with A_0 fitted to maximize agreement with the observed wave vector. **d** Growth rate from model #4 versus fitted eddy viscosity/diffusivity A_0. For the point marked ◁, the optimal value $A_0 = 0$ does not fit on the logarithmic scale

this case, the eddy viscosity needed to bring the growth rate to zero is $A_0 = 0.26\mathrm{m^2\,s^{-1}}$ (Fig. 12a).

The difference in effect between tree fluxes and turbulence is not unexpected. The tree fluxes are modeled as Rayleigh damping terms, which have no scale dependence. In contrast, the turbulence effects are modeled using Laplacian operators, which act more strongly on small-scale structures.

3.3.2 Statistical Analysis of 39 Events

We now apply our four LSA models described in Sect. 3.2 to the full ensemble of 39 canopy wave events for which subjective estimates of the phase propagation speed, direction. wavelength and period are available (M17). The TG model gives growth rates between $0.018\,\mathrm{s^{-1}}$ and $0.083\,\mathrm{s^{-1}}$, with a median value $0.036\,\mathrm{s^{-1}}$. The addition of trees (model #2) reduces the
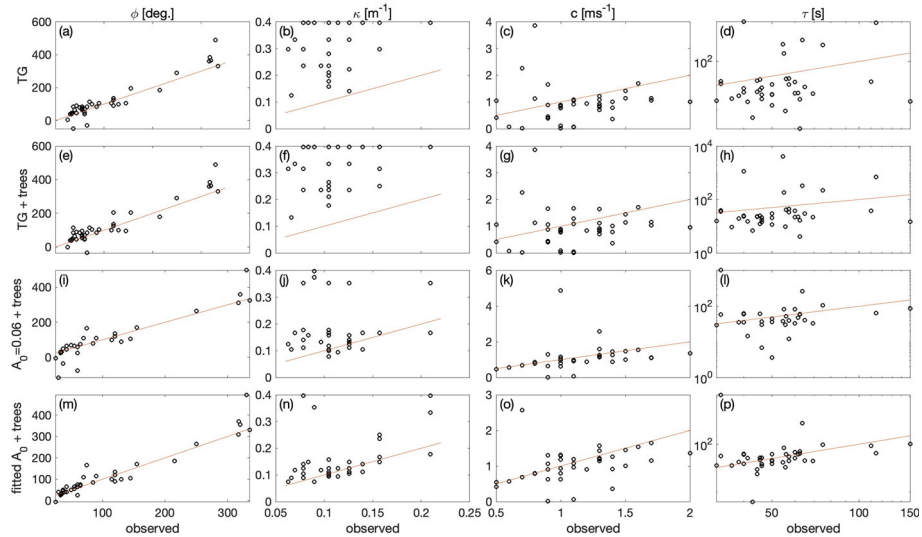
Fig. 14 Predicted versus observed wave parameters for four LSA models. Table 1 gives the corresponding comparisons in quantitative form

median growth rate to 0.032, a reduction of 12% (Fig. 13a). The further addition of viscosity with $A_0 = 0.06 \text{m}^2 \text{s}^{-1}$ (model #3; Fig. 13b) creates a general decrease in growth rate, with median reduced by more than a factor of two. Replacement of the fixed value $A_0 = 0.06 \text{m}^2 \text{s}^{-1}$ with the individually fitted values (model #4; Fig. 13c) reduces the median growth rate by a further factor of two. The optimal eddy viscosity values delivered by model #4 range from zero to $0.3 \text{m}^2 \text{s}^{-1}$, with larger values tending to produce smaller growth rates (Fig. 13d).

The optimal values of A_0 have median $0.06 \text{m}^2 \text{s}^{-1}$, and quartiles 0.03 and $0.14 \text{m}^2 \text{s}^{-1}$. These ranges are strikingly similar to the range of measured values at the shear maximum (Sect. 2.4). However, there is little correlation between measured and inferred values for individual cases.

We next compare the wave vector, phase speed and period computed using the four linear models with the subjective estimates of M17. The results shown previously for case #40 (Sect. 3.3.1) turn out to be generally true. We begin by discussing the TG, with reference to the top row of Fig. 14, and the third column of Table 1. The direction of propagation of the fastest-growing instability is reasonably consistent with that of the observed wave (Fig. 14a). This is close to the direction of maximum shear, consistent with KHI theory (e.g., Smyth and Carpenter 2019). The median of the observed directions (Table 1, row 4) is 65° north of east, whereas the median of the LSA predictions (row 5, column 3) is 85°, i.e. the prediction is high by 20°, or 31% relative to the observed value (row 6). By coincidence, the median discrepancy in individual cases (computed as median absolute difference between predicted and observed directions; row 7) is also 20°.

The approximate agreement found for the propagation direction is not found in the case of the wavenumber κ (Fig. 14b, Table 1, column 3, rows 8–11). Instead, both the difference of medians and the spread are greater than a factor of two, as was illustrated previously for case #40 (Fig. 9c). Points clustered at the top of Fig. 14b have $\kappa = 0.4 \text{m}^{-1}$, the largest

Table 1 Comparison of observed and computed wave scales using four LSA models

Model		1	2	3	4
ϕ [deg.]	<obs.>	65			
	<LSA>	85	90	75	75
	<LSA> − <obs.>	20 (31%)	25 (38%)	10 (15%)	10 (15%)
	< |LSA-obs.| >	20 (31%)	25 (38%)	15 (23%)	10 (15%)
κ [m^{-1}]	<obs.>	0.105			
	<LSA>	0.396	0.396	0.158	0.125
	<LSA> − <obs.>	0.291 (279%)	0.291 (279%)	0.053 (50%)	0.020 (20%)
	< |LSA-obs.| >	0.239 (229%)	0.239 (229%)	0.039 (38%)	0.020 (19%)
c [ms^{-1}]	<obs.>	1.100			
	<LSA>	0.898	0.888	1.061	1.067
	<LSA> − <obs.>	−0.202 (−18%)	−0.212 (−19%)	−.039 (−4%)	−0.033 (−3%)
	< |LSA-obs.| >	0.440 (40%)	0.461 (42%)	0.160 (15%)	0.138 (13%)
τ [s]	<obs.>	50			
	<LSA>	26	23	41	51
	<LSA> − <obs.>	−24 (−48%)	−27 (−54%)	−9 (−18%)	1 (2%)
	< |LSA-obs.| >	29 (58%)	30 (59%)	23 (45%)	11 (22%)

Models are defined by parameters A_0, C_d and C_h. For each wave parameter ϕ, κ, c and τ, rows give the median (denoted by angle brackets) of the observations, the median of the computed values, the systematic discrepancy (computed as the difference of the medians) and typical discrepancy in individual cases (median of absolute differences). Differences are also given, in parentheses, as a percentage of the observed median

value included in the analysis. The true value is even larger, i.e. further from the observed wavenumber.

The median phase propagation speed c (Table 1, rows 12–15) is low by 18% while individual cases typically differ by 40%. The period (rows 16–19) is systematically low by 48% while individual values differ by 58%.

To summarize: the TG model reproduces the direction well and the speed to within a few tens of percent, both in the median and in individual cases, but it overestimates the wavenumber (and underestimates the period) by more than a factor of two. This suggests that canopy waves are *not* well represented by KHI, at least not in its classical, inviscid form. We now ask whether the agreement can be improved by accounting for air-tree fluxes and ambient turbulence using the parameterizations described above.

Adding the tree fluxes alone (model #2) does not improve the correspondence with observations (Table 1, column 4). In particular, the extreme discrepancy in the wavenumber is unchanged. In other cases, the discrepancies are actually slightly greater.

We turn next to the effect of eddy viscosity/diffusivity due to ambient turbulence. To begin, we add turbulent viscosity and diffusivity at the level of $A_0=0.06\,\text{m}^2\,\text{s}^{-1}$, approximately the median of the measured values at treetop height (Fig. 8), i.e. model #3. Results may be found in Fig. 14, third row, and column 5 of table 1. All discrepancies are now significantly reduced. In particular, the discrepancy in wavenumber is reduced from a factor of two to a few tens of percent (table 1, rows 10,11).

These promising results conceal a serious deficiency. In 6 of the 39 cases studied, the stability analysis failed to yield a growing mode. The highest growth rate was either less than the cutoff value $0.0033\,\text{s}^{-1}$ or negative, indicating that the value $A_0 = 0.06\,\text{m}^2\,\text{s}^{-1}$ is beyond the stability boundary. This is a serious failure since the REAL images clearly show an instability. There are multiple possible reasons for this. For example, the waves may have grown slowly enough that their properties were determined by events more than 5 min previous to their becoming visible. Alternatively, the variation of eddy viscosity and diffusivity with height, neglected here, may be important. But the most likely explanation, is that the single value $A_0 = 0.06\,\text{m}^2\,\text{s}^{-1}$ is not applicable in all cases, and is even beyond the stability limit for some. We now seek to remedy that problem.

In model #4, we employ for each case the value of A_0 that optimizes the correspondence in the wave vector. When the stability analysis is conducted using these optimal values (table 1, bottom row and Fig. 14, right-hand column), the discrepancies from the observations are generally (though not always) smaller than in the case $A_0 = 0.06\,\text{m}^2\text{s}^{-1}$. The improved agreement in the wave vector is to be expected, but not so the agreement in the phase speed, since no effort has been made to optimize the latter. Most importantly, though, the comparison is now valid (i.e. apples-to-apples) because growing modes were found in all cases where canopy waves were observed.

4 Conclusions

Applying linear stability theory to boundary layer observations made over an orchard, we have explored the relationship between canopy waves and KHI. Our results support two main conclusions:

– Canopy waves may be understood as KH billows only when the effects of ambient turbulence are accounted for.

– Canopy waves occur in relatively calm conditions where ambient turbulence is weak enough to permit their growth. This state is often reached just before sunrise.

Besides the inevitable measurement errors, discrepancies between theory and observations may result from three main shortcomings of the analysis.

– Questionable assumptions underlie the linear stability analyses, e.g. perturbations from parallel flow are not truly infinitesimal and the background flow is neither steady nor horizontally homogeneous. Unsteadiness may be addressed by looking for optimal transient modes of instability (Kaminski et al. 2014), while inhomogeneity requires a nonmodal approach such as large-eddy simulation (Moeng and Sullivan 2014; Patton et al. 2016).
– The present analyses ignore the vertical variation of turbulence, which generally peaks at treetop height, an extension that will be implemented in the future.
– Our estimates of wavelength, period and phase velocity from REAL imagery are subjective. They were a first attempt to capture the case to case variability, ignoring in particular the spatial and temporal variability that may occur within a given case. Objective methods are now under study.

Canopy waves are a significant factor in the regulation of atmospheric properties in forest canopies, especially at night or over cold surfaces, for example, at high latitudes in winter. Those properties include temperature and trace gases such as water vapor, methane, and carbon dioxide (Fitzjarrald and Moore 1990). KHI represents a more general class of phenomena which create and maintain turbulent fluxes in diverse geophysical fluid environments including oceans (Smyth and Moum 2012; Smyth 2020), estuaries (Tedford et al. 2009; Geyer et al. 2010) and the magnetospheres of Earth and other planets (Michael et al. 2021) as well as the atmosphere. The identification of canopy waves as a form of KHI suggests that, besides their intrinsic importance, forest canopies can provide a natural laboratory where KHI occurs predictably and is readily accessible for study. Topics for future study include comparison of the breaking mechanisms suggested by the asymmetric structure of observed billows with predictions from direct simulations of KHI (e.g.,Espinoza-Ruiz et al. 2023; Mashayek and Peltier 2012a, b), and comparison of length scale ratios that characterize billow geometry with values found in the ocean (Smyth and Moum 2000).

Data Availability The datasets generated and/or analysed during the current study, along with the computer codes used, are available from the corresponding author upon reasonable request. Linear stability analysis codes may be downloaded from https://blogs.oregonstate.edu/salty/.

Declarations

Conflict of Interest The authors are aware of no conflicts of interest.

Appendix 1: A Linear, Normal-Mode Stability Analysis of Stratified, Parallel Shear Flows Including Ambient Turbulence and Vegetation Effects

For a small-amplitude, normal mode disturbance with horizontal wave vector $\mathbf{k}$ evolving on a steady, parallel, horizontal background flow $\mathbf{u}_h$, mode evolution is determined solely by the component of the background flow parallel to the wave vector. Therefore, for a given $\mathbf{k}$, we consider the two-dimensional problem of a parallel shear flow $U(z) = \mathbf{k} \cdot \mathbf{u}_h / \kappa$ disturbed by the velocity perturbation $\{u', w'\}$ and the buoyancy perturbation b'. Applying the Boussinesq approximation, density is decomposed as $\rho = \rho_0 + \bar{\rho}(z) + \rho'(x, z, t)$, after which the buoyancy, $b = g(\rho_0 - \rho)/\rho_0$, becomes $b = B(z) + b'$, where $B = -g\bar{\rho}/\rho_0$ and $b' = -g\rho'/\rho_0$. In this context the primed quantities are treated as small perturbations.

Viscosity and diffusivity may be molecular in origin, or they may represent the effects of turbulence on spatial scales much smaller than the wave scale κ^{-1}. Following (Liu et al. 2012), the viscosity and diffusivity are allowed to have separate horizontal $\{A_h, K_h\}$ and vertical $\{A_v, K_v\}$ parts, and to vary in the vertical.

We also parameterize the transfer of momentum and buoyancy between the vegetation and the flow perturbation following (Lee 1997). The Boussinesq equations, linearized about the background flow, are then:

$$\frac{\partial u'}{\partial t} + U\frac{\partial u'}{\partial x} + w'\frac{dU}{dz} = -\frac{\partial \pi'}{\partial x} + A_h\nabla_h^2 u' + \frac{\partial}{\partial z}\left(A_v\frac{\partial u'}{\partial z}\right) - C_d L_f |U|u', \tag{7}$$

$$\frac{\partial w'}{\partial t} + U\frac{\partial w'}{\partial x} = -\frac{\partial \pi'}{\partial z} + b' + A_h\nabla_h^2 w' + \frac{\partial}{\partial z}\left(A_v\frac{\partial w'}{\partial z}\right) - C_d L_f |U|w', \tag{8}$$

$$\frac{\partial b'}{\partial t} + U\frac{\partial b'}{\partial x} + w'\frac{dB}{dz} = K_h\nabla_h^2 b' + \frac{\partial}{\partial z}\left(K_v\frac{\partial b'}{\partial z}\right) - C_h L_f |U|b', \tag{9}$$

where x is the horizontal coordinate parallel to $\mathbf{k}$. The final term in each equation is the parameterized flow-vegetation flux (Lee 1997). The coefficients C_d and C_h are constants while plant area density L_f varies with height.

For the present application, the turbulence is assumed to be isotropic and to have Prandtl number unity, so that $A_v = K_v = A_h = K_h$. The coefficients C_d and C_h are either $\{0.15, 0.10\}$ or zero. The vertical structure of L_f is given by (6).

Perturbations u', w' and b' are assumed to have the normal mode form (2). The linearized normal-mode equations are then written as a generalized differential eigenvalue problem:

$$\sigma\begin{bmatrix} \nabla^2 & 0 \\ 0 & 1 \end{bmatrix}\begin{bmatrix} \hat{w} \\ \hat{b} \end{bmatrix} = \begin{bmatrix} -\iota k U\nabla^2 + \iota k\frac{d^2 U}{dz^2} + T_w + V_w & -k^2 \\ -\frac{dB}{dz} & -\iota k U + T_b + V_b \end{bmatrix}\begin{bmatrix} \hat{w} \\ \hat{b} \end{bmatrix}, \tag{10}$$

where

$$\nabla^2 = \frac{d^2}{dz^2} - k^2, \tag{11}$$

is the Laplacian in normal-mode form. The operators expressing viscous and diffusive effects of turbulence are:

$$T_w = \frac{d^2}{dz^2}\left(A_v \frac{d^2}{dz^2}\right) - k^2 \frac{d}{dz}\left[(A_h + A_v)\frac{d}{dz}\right] + k^4 A_h \tag{12}$$

$$T_b = \frac{d}{dz}\left(K_v \frac{d}{dz}\right) - k^2 K_h, \tag{13}$$

while vegetation effects are represented by:

$$V_w = -C_d \frac{d}{dz}\left[L_f |U| \frac{d}{dz}\right] + k^2 C_d L_f |U|, \tag{14}$$

$$V_b = -C_h L_f |U|. \tag{15}$$

In the inviscid, nondiffusive, zero-vegetation limit $A_h = K_h = A_v = K_v = C_d = C_h = 0$, (10) reduces to the TG equation. Specification of the problem is completed by the imposition of a rigid, impermeable boundary $\hat{w} = 0$, $d\hat{w}/dz = 0$ at the surface $z = 0$ and a frictionless boundary $\hat{w} = d^2\hat{w}/dz^2 = 0$ at $z = 50$ m. Buoyancy is fixed ($\hat{b} = 0$) at both boundaries.

The problem is solved on a stretched grid with minimum spacing 0.35 m between 10 and 30 m height and maximum 2 m in an upper sponge layer between 30 m and 50 m. Approximating z-derivatives as sixth-order finite differences, we convert the differential eigenvalue problem (10), together with the boundary conditions, to an algebraic eigenvalue problem as described by Lian et al. (2020). The eigenvalue problem is solved using standard numerical methods.

References

Arnqvist J, Bergström H, Nappo C (2016) Examination of the mechanism behind observed canopy waves. Agric For Meteorol 218:196–203

Bailey BN, Stoll R (2016) The creation and evolution of coherent structures in plant canopy flows and their role in turbulent transport. J Fluid Mech 789:425–460

Blumen W, Banta R, Burns SP, Fritts DC, Newsom R, Poulos GS, Sun J (2001) Turbulence statistics of a Kelvin-Helmholtz billow event observed in the night-time boundary layer during the Cooperative Atmosphere-Surface Exchange Study field program. Dyn Atmos Oceans 34(2):189–204

Browning KA, Watkins CD (1970) Observations of clear air turbulence by high power radar. Nature 227:260–263

Carpenter J, Tedford E, Heifetz E, Lawrence G (2013) Instability in stratified shear flow: review of a physical interpretation based on interacting waves. Appl Mech Rev 64:6. https://doi.org/10.1115/1.4007909

Caulfield CP, Peltier WR (1994) Three dimensionalization of the stratified mixing layer. Phys Fluids 6(12):3803–3805. https://doi.org/10.1063/1.868370

Cava D, Giostra U, Siqueira M, Katul G (2004) Organised motion and radiative perturbations in the nocturnal canopy sublayer above an even-aged pine forest. Boundary-Layer Meteorol 112:129–157

Chapman D, Browning KA (1997) Radar observations of wind-shear splitting within evolving atmospheric Kelvin-Helmholtz billows. Q J R Meterol Soc 123(541):1433–1439

De Baas AF, Driedonks AGM (1985) Internal gravity waves in a stably stratified boundary layer. Boundary-Layer Meteorol 31(3):303–323

Einaudi F, Finnigan JJ (1981) The interaction between an internal gravity wave and the planetary bounary layer. Part I: The linear analysis. Q J R Meterol Soc 107:793–806

Emmanuel CB (1973) Richardson number profiles through shear instability wave regions observe in the lower planetary boundary layer. Boundary-Layer Meteorol 5:19–27

Emmanuel CB, Bean BR, McAllister LG, Pollard JR (1972) Observations of Helmholtz waves in the lower atmosphere with an acoustic sounder. J Atmos Sci 29(5):886–892

Espinoza-Ruiz A, Mayor SD, Smyth WD (2023) Evidence of atmospheric canopy wave breaking in scanning aerosol lidar images. In: Poster at 24th Symposium on Boundary Layers and Turbulence, American Meteorological Society, Denver, CO

Finnigan J (2000) Turbulence in plant canopies. Ann Rev Fluid Mech 32(1):519–571

Finnigan JJ, Einaudi F, Fua D (1984) The interaction between an internal gravity wave and turbulence in the stably-stratified nocturnal boundary layer. J Atmos Sci 41(16):2409–2436

Fitzjarrald DR, Moore KE (1990) Mechanisms of nocturnal exchange between the rain forest and the atmosphere. J Geophys Res 95(D10):16839–16850

Geyer W, Lavery A, Scully M, Trowbridge J (2010) Mixing by shear instability at high Reynolds number. Geophys Res Lett. https://doi.org/10.1029/2010GL045272

Gossard EE, Richter JH, Atlas D (1970) Internal waves in the atmosphere from high-resolution radar measurements. J Geophys Res 75(18):3523–3536

Hooke WH, Hall FF, Gossard EE (1973) Observed generation of an atmospheric gravity wave by shear instability in the mean flow of the planetary boundary layer. Boundary-Layer Meteorol 5:29–41

Howard L (1961) Note on a paper of John W. Miles. J Fluid Mech 10:509–512

Kaimal JC, Finnigan JJ (1994) Atmospheric boundary layer flows. Oxford University Press

Kaminski AK, Smyth WD (2019) Stratified shear instability in a field of pre-existing turbulence. J Fluid Mech 863:639–658

Kaminski AK, Caulfield CP, Taylor JR (2014) Transient growth in strongly stratified shear layers. J Fluid Mech 758(4)

Kelvin L (1871) Stratified shear instability in a field of pre-existing turbulence. Phil Mag 10:155–168

Klaassen GP, Peltier WR (1985) The onset of turbulence in finite-amplitude Kelvin–Helmholtz billows. J Fluid Mech 155:1–35. https://doi.org/10.1017/S0022112085001690

Klaassen GP, Peltier WR (1989) The role of transverse secondary instabilities in the evolution of free shear layers. J Fluid Mech 202:367–402

Klaassen GP, Peltier WR (1991) The influence of stratification on secondary instability in free shear layers. J Fluid Mech 227:71–106. https://doi.org/10.1017/S0022112091000046

Lee X (1997) Gravity waves in a forest: a linear analysis. J Atmos Sci 54:2574–2585

Lee X, Black TA, den Hartog G, Neumann HH, Nesic Z, Olejnik J (1996) Carbon dioxide exchange and nocturnal processes over a mixed deciduous forest. Agric Forest Meterol 81(1):13–29

Lee X, Neumann HH, Hartog GD, Fuentes JD, Black TA, Mickle RE, Yang PC, Blanken PD (1997) Observation of gravity waves in a boreal forest. Boundary-Layer Meteorol 84:383–398

Li L, Smyth WD, Thorpe SA (2015) Destabilization of a stratified shear layer by ambient turbulence. J Fluid Mech 771:1–15

Lian Q, Smyth WD, Liu Z (2020) Numerical computation of instabilities and internal waves from in situ measurements via the viscous taylor-goldstein problem. J Atmos Ocean Technol 37(5):759–776

Liu CL, Kaminski A, Smyth W (2022) The butterfly effect and the transition to turbulence in a stratified shear layer. J Fluid Mech 953:A43. https://doi.org/10.1017/jfm.2022.985

Liu Z, Thorpe S, Smyth W (2012) Instability and hydraulics of turbulent stratified shear flows. J Fluid Mech 695:235–256

Mashayek A, Peltier WR (2012) The 'zoo' of secondary instabilities precursory to stratified shear flow transition. part 1 shear aligned convection, pairing, and braid instabilities. J Fluid Mech 708:5–44

Mashayek A, Peltier WR (2012) The 'zoo' of secondary instabilities precursory to stratified shear flow transition. part 2 the influence of stratification. J Fluid Mech 708:45–70

Maslowe SA (1973) Finite-amplitude Kelvin–Helmholtz billows. Boundary-Layer Meteorol 5:43–52

Mayor SD (2017) Observations of microscale internal gravity waves in very stable atmospheric boundary layers over an orchard canopy. Agric For Meteorol 244–245:136–150

Mayor SD, Spuler SM, Morley BM, Loew E (2007) Polarization lidar at 1.54-microns and observations of plumes from aerosol generators. Opt Eng. https://doi.org/10.1117/1.2786406

Michael AT, Sorathia KA, Merkin VG, Nykyri K, Burkholder B, Ma X, Ukhorskiy AY, Garretson J (2021) Modeling Kelvin-Helmholtz instability at the high-latitude boundary layer in a global magnetosphere simulation. Geophys Res Lett. https://doi.org/10.1029/2021GL094002

Mifsud KE, Iqbal M, Dérian P, Mayor SD, Mayor SD (2021) Objective determination of wavelength and orientation of atmospheric canopy waves. In: Poster A45C-1867 at Fall meeting of the American Geophysical Union, New Orleans, LA

Miles J (1961) On the stability of heterogeneous shear flows. J Fluid Mech 10:496–508

Moeng CH, Sullivan PP (2014) Large eddy simulation. In: North G, Zhang F, Pyle J (eds) Encyclopedia of atmospheric sciences, 2nd edn. Academic Press, pp 232–240

Newsom RK, Banta RM (2003) Shear-flow instability in the stable nocturnal boundary layer as observed by doppler lidar during cases-99. J Atmos Sci 60(1):16–33

Patton EG, Horst TW, Sullivan PP, Lenschow DH, Oncley SP, Brown WOJ, Burns SP, Guenther AB, Held A, Karl T, Mayor SD, Rizzo LV, Spuler SM, Sun J, Turnipseed AA, Allwine EJ, Edburg SL, Lamb BK,

Avissar R, Calhoun R, Kleissl J, Massman WJ, U KTP, Weil JC, (2011) The Canopy Horizontal Array Turbulence Study (CHATS). Bull Amer Meteor Soc 92:593–611

Patton EG, Sullivan PP, Shaw RH, Finnigan JJ, Weil JC (2016) Atmospheric stability influences on coupled boundary layer and canopy turbulence. J Atmos Sci 73(4):1621–1647

Petenko I, Mastrantonio G, Viola A, Argentini S, Pietroni I (2012) Wavy vertical motions in the ABL observed by sodar. Boundary-Layer Meteorol 143:125–141

Pulido M, Chimonas G (2001) Forest canopy waves: The long-wavelength component. Boundary-Layer Meteorol 100(2):209–224

Raupach MR, Thom AS (1981) Turbulence in and above plant canopies. Ann Rev Fluid Mech 13:97–129

Raupach MR, Finnigan JJ, Brunet Y (1996) Coherent eddies and turbulence in vegetation canopies: the mixing-layer analogy. Boundary-Layer Meteorol 78:351–382

Richter JH (1969) High resolution tropospheric radar sounding. Radio Sci 4(12):1261–1268

Smyth W (2020) Marginal instability and the efficiency of ocean mixing. J Phys Oceanogr 50(8):2141–2150

Smyth W, Moum J, Li L, Thorpe S (2013) Diurnal shear instability, the descent of the surface shear layer, and the deep cycle of equatorial turbulence. J Phys Oceanogr 43:2432–2455

Smyth WD, Carpenter JR (2019) Instability in Geophysical Flows. Cambridge University Press

Smyth WD, Moum JN (2000) Length scales of turbulence in stably stratified mixing layers. Phys Fluids 12:1327–1342

Smyth WD, Moum JN (2012) Ocean mixing by Kelvin–Helmholtz instability. Oceanography 25(2):140–149

Sun J, Mahrt L, Nappo C, Lenschow DH (2015) Wind and temperature oscillations generated by wave-turbulence interactions in the stably stratified boundary layer. J Atmos Sci 72(4):1484–1503

Tedford EW, Carpenter JR, Pawlowicz R, Pieters R, Lawrence GA (2009) Observation and analysis of shear instability in the Fraser River estuary. J Geophys Res 114:C11006. https://doi.org/10.1029/2009JC005313

Thorpe S, Smyth W, Li L (2013) The effect of small viscosity and diffusivity on the marginal stability of stably stratified shear flows. J Fluid Mech 731:461–476

Tong C, Ding M (2020) Velocity-defect laws, log law and logarithmic friction law in the convective atmospheric boundary layer. J Fluid Mech 883:A36

von Helmholtz H (1890) Die energie der wogen und des windes. Annalen der Physik 277(12):641–662

Winant CD, Browand FK (1974) Vortex pairing: the mechanism of turbulent mixing-layer growth at moderate reynolds number. J Fluid Mech 63:237–255

Zaremba LL, Carroll JJ (1999) Summer wind flow regimes over the Sacramento Valley. J Appl Meteorol 38:1463–1473